Photonic Sensors (2012) Vol. 2, No. 2: 97–117

DOI: 10.1007/s13320-012-0057-4 **Photonic Sensors**

Review

OFS Research Over the Last 10 Years at CQU & UESTC

Yunjiang RAO

Key Laboratory of Optical Fiber Sensing & Communications (Ministry of Education), University of Electronic Science and Technology of China, Chengdu, 611731, China

*Corresponding author, Yunjiang RAO E-mail: yjrao@uestc.edu.cn

Abstract: This article reviews my new optical fiber sensing (OFS) research activities in China for the last ten years at Chongqing University and University of Electronic Science and Technology of China, since I returned from UK in 1999. The research progress in long period fiber gratings (LPFGs), distributed fiber sensing systems and microfiber sensors is introduced. For LPFGs, the processing method with high-frequency CO_2 laser pulses types of LPFGs fabricated and the related applications for both optical sensing and optical communication are described. For distributed fiber sensing systems, the fiber-optic polarization optical time domain reflectometer (POTDR), fiber-optic phase-sensitive optical time domain reflectometer (Φ-OTDR) and Brillouin optical time-domain analyzer (BOTDA) are developed, respectively. For microfiber sensors, we mainly focus on the knot resonator and its application for sensing of the refractive index and acceleration, etc.

Keywords: Fiber optic sensor, long period fiber grating, BOTDA, microfiber

1. Introduction

In my last review paper, "Studies on fiber optic low-coherence interferometry and fiber Brag grating sensors" [1], I mainly introduced our work at the University of Kent as well as the follow-up work after I returned to China. But the story does not end yet; this paper continues to introduce some other optical fiber sensing (OFS) research activities of my group. During the recent ten years in China, we have made important progress in studies of long-period fiber grating (LPFG) sensors, distributed fiber-optic sensors and microfiber sensors. A systematic review of these advances is given in the successive part of this paper.

Generally speaking, there are two types of in-fiber gratings: fiber Bragg gratings (FBGs) with periodicities of the order of the optical wavelength and LPFGs with periods of several hundred wavelengths. Compared with FBGs, LPFGs have many special characteristics, such as simplicity of fabrication, low back reflection, low insertion loss and high sensitivity with regards to temperature, bend, and torsion. Thus, LPFGs have been used as band-rejection filters, fiber amplifier gain equalizers, broadband couplers, and also as sensors for the measurement of a wide range of physical and chemical parameters. Several methods, such as ultraviolet (UV) laser exposure, electrical arcing, CO_2 laser irradiation, etching and carving, have been reported to fabricate LPFGs. Based on the CO_2 laser processing method, we developed a series of LPGFs for applications of both optical communication and optical fiber sensing. These results are introduced in Section 2.

Distributed optical fiber sensing systems utilize the optical fiber itself as both transmission medium

Received: 11 November 2011 / Revised version: 28 February 2012

and sensing medium, and they can obtain simultaneously both spatial and temporal information along the entire length of a fiber. Thus, they have great potential for use in civil structures, environmental monitoring, aerospace industry, and geotechnical engineering etc. Since the phase and polarization of the transmission light are sensitive to perturbations, the fiber-optic polarization optical time domain reflectometer (POTDR) and the fiber-optic phase-sensitive optical time domain reflectometer (Φ-OTDR) are used for distributed sensing. Another type of distributed fiber sensors based on the Brillouin scattering, i.e., Brillouin optical time-domain analyzer (BOTDA), can be used for measuring the temperature/strain along a fiber by finding the changes in the Brillouin frequency shift. Our recent works on these three types of distributed fiber sensors will be introduced in Section 3.

In the research area of fiber sensors, the microfiber also attracts significant attention. These novel types of fibers with diameters close to or smaller than the wavelength of the guided lightwave are capable of offering large fractions of evanescent waves and high-intensity surface fields, making them highly sensitive to the index change in the surrounding medium, because of the significantly enhanced interaction between the guided lightwave and surrounding specimens. In addition, microfibers can be readily bended or twisted to form high-Q resonators and interferometers. By making use of these characteristics, we developed highly-sensitive microfiber sensors for the measurement of the temperature, acceleration and refractive index. The results will be given in Section 4.

2. Studies on LPFGs

2.1 Manufacture of LPFGs using high-frequency CO_2 lasers pulses

Compared with other methods (e.g., UV-writing method), the CO_2 laser irradiation method does not need doping of the photosensitive material in the fiber, therefore it can be applied practically to any type of fiber and can write thermally stable gratings. Based on the high-frequency CO_2 laser processing, we developed a novel 2D writing system for fabrications of various kinds of LPFGs, including LPFGs in conventional single-mode fibers (SMF), in specially doped fibers, in twisted fibers, and in photonic crystal fibers (PCF) *et al*. [2–10].

2.1.1 LPFGs in normal single mode fibers

One typical CO_2 laser writing method of LPFGs developed by us is shown in Fig. 1. The fiber is scanned by the CO_2 laser at both X-Y axes by means of a two-dimensional optical scanner attached to the laser head [2]. In terms of the fabrication process, the focused high-frequency CO_2 laser beam is scanned along the X direction at a location near the edge area of the cladding, forming the first grating period. Then, the CO_2 laser beam is moved by a grating period along the Y direction to write the next grating period. Once all the grating periods are written, the LPFG is finished. We call this whole process a scanning circle. Several scanning circles can be adopted to obtain specific grating profiles.

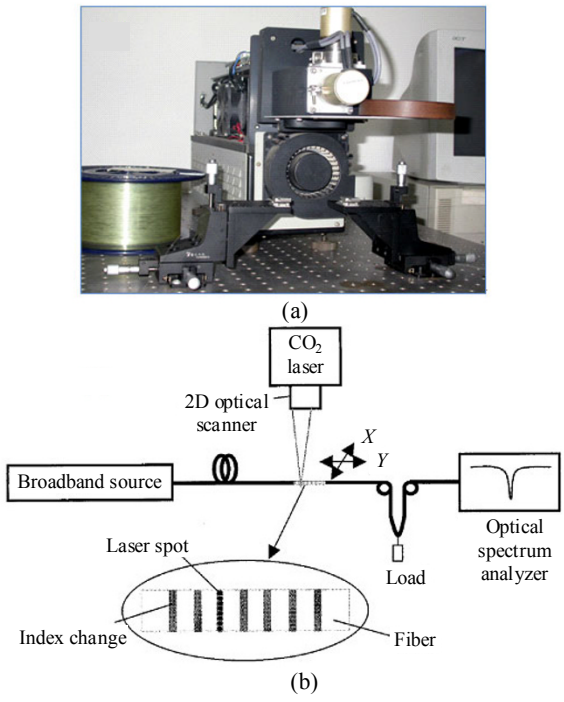

Fig. 1 High-frequency CO_2 laser processing system: (a) the photograph and (b) the schematic diagram [2].

A. LPFGs without physical deformation in the fiber

As we know, silica glass has a strong absorption around the wavelength of the CO_2 laser, so the incident light intensity is gradually weakened along the incident direction, which is likely to result in an asymmetric index change within the cross section of the fiber [3].

If the dose of the CO_2 laser beam focused on the fiber is set to a moderate value, LPFGs can be fabricated through modulation of the refractive index in the fiber without any physical deformation. As shown in Figs. 2(a) and 2(b), the index change on the incident side is larger than that on the opposite side. Hence, strong coupling would occur between the fundamental core mode and the higher order asymmetric cladding modes, and this grating structure should have high sensitivity to environmental changes.

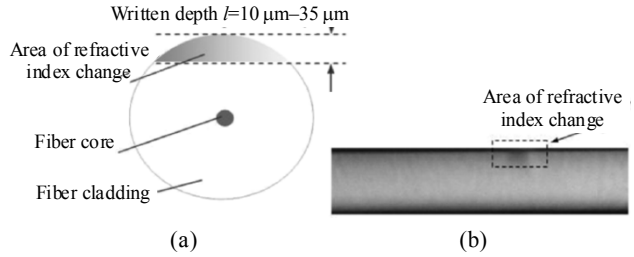

Fig. 2 Refractive index variation on the cross section of the edge written LPFG.: (a) the schematic diagram and (b) the observed fiber image via an optical microscope [3].

During the writing process of LPFGs, the area of refractive index modulation along the fiber axis is extended. As a result, the duty cycle becomes larger, and the resonant wavelength of the LPFG shifts towards a shorter wavelength. However, the shift is very small, seeing Fig. 3(a). The comparison between Figs. 3(a) and 3(b) indicates that the resonant wavelength shifts toward the shorter wavelength, and the resonance peak amplitude of the LPFG with a relatively large writing depth is much bigger than that of the LPFG with a smaller writing depth under the same CO_2 laser pulse exposure condition.

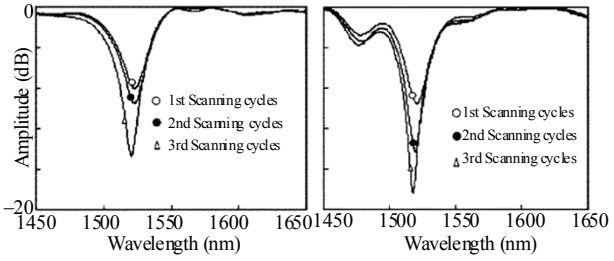

Fig. 3 Growth of the edge-written LPFG: (a) the writing depth is 15 mm and (b) the writing depth is 35 mm [3].

B. LPFGs with periodic grooves on the fiber

By increasing the energy of the focused CO_2 laser beam, the SiO_2 on the surface of the fiber can be gasified due to a creation of local high temperature. In this way, periodic grooves can be carved on the fiber, creating an LPFG as shown in Fig. 4 [4].

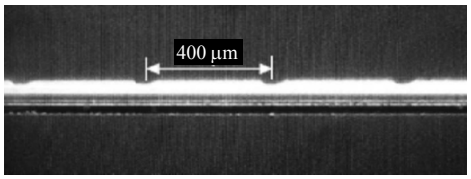

Fig. 4 Photograph of the CO_2-laser-carved LPFG [4].

The schematic diagram of the CO_2-laser-carved LPFG is also shown in Fig. 5(a). When such an LPFG is stretched longitudinally, periodic microbending will be induced in the grooved section of the fiber, seeing Fig. 5(b). The stretch-induced microbends can effectively enhance the refractive index modulation in the LPFGs.

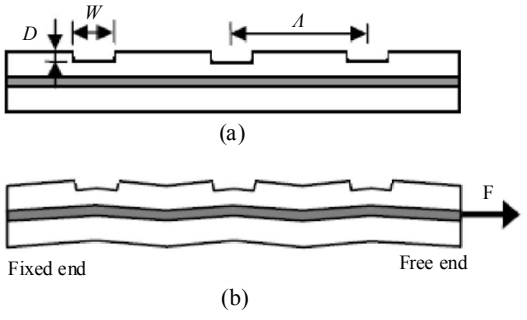

Fig. 5 Schematic diagram of the CO_2-laser-carved LPFG: (a) before and (b) after a stretching force F is applied [4].

From Fig. 6, we can find that the resonant wavelength shifts toward the shorter wavelength by about –12 nm, and the peak attenuation increases by

about 20 dB when a stretching force is applied. In addition, the transmission attenuation changes to the opposite direction when the tensile strain is increased beyond a critical value of about 100 με. This is due to the over coupling between the fundamental core mode and the cladding mode. With an increase in the tensile strain from 0 to 100 με, the resonant wavelength shifts from 1569.93 nm to 1559.58 nm with an extremely high average sensitivity of –102.89 nm/mε, which is much more sensitive than CO_2-laser-induced LPFGs without periodic grooves (the typical sensitivity is only about –0.45 nm/mε).

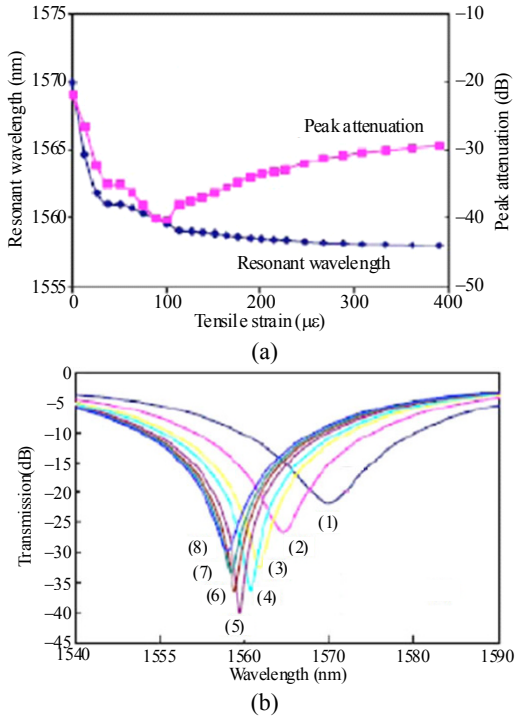

Fig. 6 Changes in the transmission spectrum for different values of the tensile strain: (a) variations of the resonant wavelength and the peak attenuation and (b) transmission spectrum evolution of the CO_2-laser-carved LPFG with the tensile strain [4] (curves marked with (1)–(8) correspond to E= 0, 12 με, 25 με, 63 με, 100 με, 150 με, 214 με and 339 με, respectively [4]).

2.1.2 LPFGs in specially doped fibers

It is known that stress relaxation is the dominant physical mechanism in the CO_2-laser-writing process of LPFGs for a conventional SMF. The writing mechanism is more complicated for a boron-doped fiber. Since the doping of boron can lower the fictive temperature of the core substantially, local heating of the fiber by CO_2 laser radiation can cause not only stress relaxation, but also glass structure changes in the core.

Figure 7 illustrates the variation of the glass volume with the glass temperature under different heating and cooling processes. The three processes A, B and C are described in Table 1. Obviously, the refractive index and the fictive temperature of the glass can be changed differently by different heating or cooling processes.

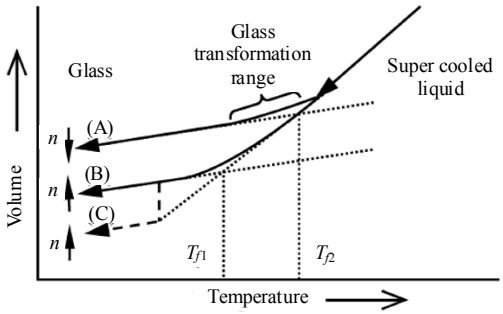

Fig. 7 Illustration of the variation of the glass volume with the glass temperature under different heating and cooling processes [5].

Table 1 Descriptions of processes A, B, and C.

Process	Starting temperature	Cooling speed	Fictive temperature	Refractive index
A	> fictive	fast	T_{f2}	decrease
B	> fictive	slow	T_{f1}	increase
C	< fictive	fast	< T_{f1}	increase

Figure 8 shows the transmission spectrum of a typical grating in an unannealed boron-doped fiber, together with an image of the near-field pattern of the coupled cladding mode (the LP_{07} mode) at the resonance wavelength of 1531 nm. The spectrum is as clean as that of a UV-written grating, and the nearfield pattern of the cladding mode is highly symmetric, which indicates that the index distribution induced by the CO_2-laser pulses is

confined in the core.

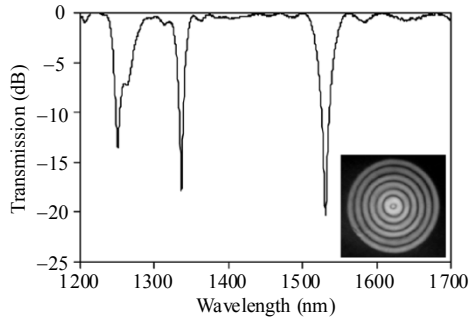

Fig. 8 Transmission spectrum of a typical CO_2-laser-written LPFG in a commercial boron-doped fiber (the inset gives the near-field pattern of the coupled LP_{07} cladding mode) [5].

The changes in the resonance wavelength for the unannealed and annealed cases of the born-doped fiber are given in Figs. 9(a) and 9(b), respectively. For the unannealed case in Fig. 9(a), the grating

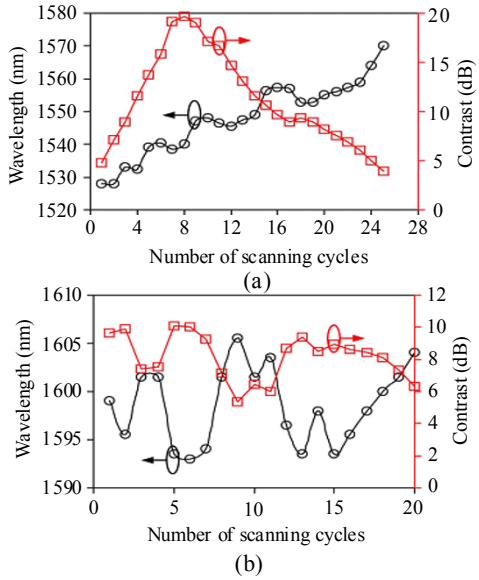

Fig. 9 Variations of the resonance wavelength and the grating contrast with the number of scanning cycles for a grating written in an unannealed fiber [(a)] and in the fiber annealed at 400 ℃ [(b)].

contrast increases first with the number of scanning cycles and then decreases after reaching the maximum. The resonance wavelength moves consistently to the longer wavelength due to the change in the glass structure in the core. Additionally, the fluctuations in the resonance wavelength imply a small counteracting effect against the monotonous trend of moving towards the longer wavelength. The counteracting effect must produce a negative change in the core index, which suggests the effect of stress relaxation.

For the annealed case in Fig. 9(b), large variations with the number of scanning cycles are observed. It is due to the interplay of the volume increase and glass densification in the core, i.e., a combined process of regimes A and C shown in Fig. 7.

We also proposed the writing of apodized phase-shifted LPFGs in a germanium-boron co-doped SMF [6]. The use of such a heavily doped fiber allows the grating to be formed in the fiber core with one-side exposure at a low CO_2 laser energy density. This grating couples light only to axially symmetric cladding modes and thus generates a clean transmission spectrum with a negligible polarization dependence. As shown in Fig. 10, the ripples between the two split rejection bands are removed by index apodization.

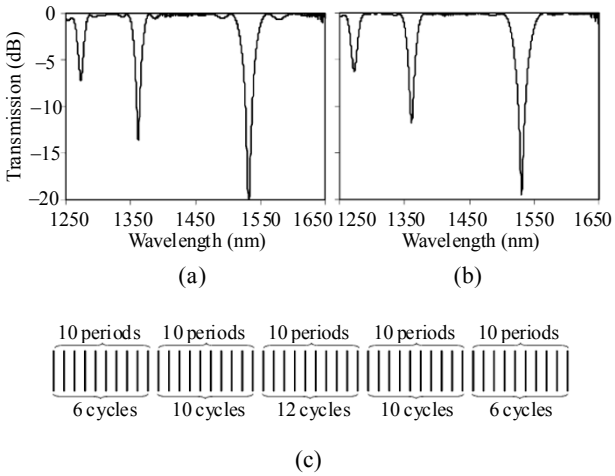

Fig. 10 Transmission spectra of (a) a uniform LPFG, (b) an index-apodized LPFG and (c) fabrication recipe for the grating in (b) [6].

2.1.3 LPFGs in twisted fibers

When writing an LPFG in a twisted fiber, since the fiber is subjected to large twisting tension during CO_2 laser irradiation, a large frozen-in strain is generated in the fiber. After the applied twist is

removed, the frozen-in strain turns into a torsion stress that rotates along the fiber. The grating written in a twisted fiber is referred to as the twisted LPFG (T-LPFG), and the grating written in a twisted fiber with the twist removed afterwards is referred to as the rotary LPFG (R-LPFG).

One setup for the fabrication of an R-LPFG is shown in Fig. 11. A fiber is mounted on a platform with its two ends fixed respectively at two holders that are separated by a distance. The fiber can be twisted by rotating a disc attached to one of the holders. The remaining process of writing an LPFG is similar to that described in Fig. 1.

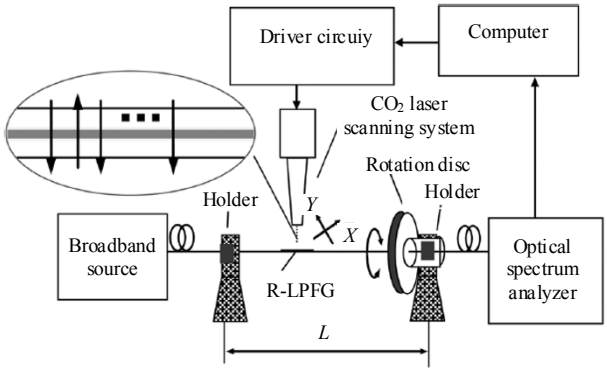

Fig. 11 Schematic diagram showing the setup for the fabrication of an R-LPFG [7].

In Fig. 12, the transmission spectrum of the T-LPFG consists of two rejection bands, which correspond respectively to the coupling to two different orders of the cladding modes. The rejection bands of the T-LPFG are insensitive to the twist rate. On the other hand, the transmission spectrum of the R-LPFG is highly sensitive to the twist rate. At a lower twist rate, the spectrum of the R-LPFG is similar to that of the corresponding T-LPFG, seeing Fig. 12(a). At a higher twist rate, each of the rejection bands is split into two, seeing Fig. 12(b). In addition, the splitting effect is polarization independent. It worth noting that the above result is accurate only when the grating is sufficiently long, compared with the twist period [7].

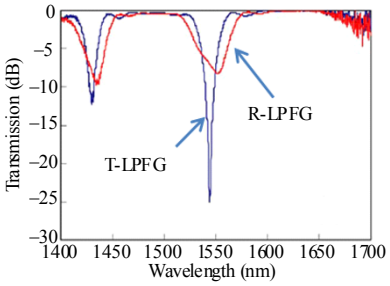

(a)

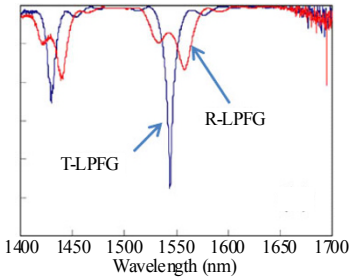

(b)

Fig. 12 Transmission spectra of R-LPFGs and the corresponding T-LPFGs fabricated with different twist rates: (a) the twist period equal to 60 mm, (b) the twist period equal to 50 mm [7].

Taking the 1550-nm rejection band of the R-LPFG as an example, we studied the influence of twist period, torsion and temperature on the wavelength separation of the two spitted dips. The results are presented in Figs. 13–15.

In Fig. 13, it is observed that the wavelength separation decreases with the twist period. In Fig. 14, the wavelength separation increases with the applied torsion when the direction of the torsion is opposite to that of the original twist applied to the fiber (i.e., negative torsion), and the wavelength separation decreases with a negative torsion.

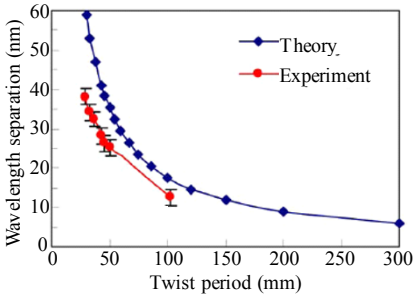

Fig. 13 Wavelength separation of the R-LPFG as a function of the twist period for the resonance at the wavelength of 1550 nm [8].

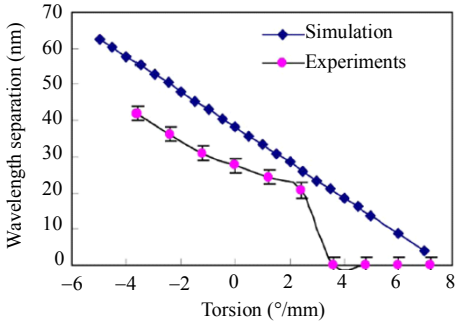

Fig. 14 Wavelength separation of the R-LPFG as a function of the torsion, where the "+" and "–" signs refer to the two opposite directions of the applied torsion [8].

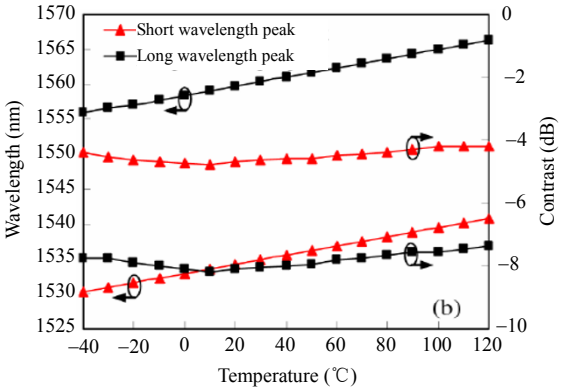

Fig. 15 Temperature response of the R-LPFG [8].

In Fig. 15, the wavelength variation of the two dips versus temperature is presented. The temperature sensitivities of the shorter and longer wavelengths, which are very close to each other, are 0.0697 nm/℃and 0.0704 nm/℃, respectively. This means that the wavelength separation is insensitivity to temperature, i.e., the sensitivity is only 0.0007 nm/℃. We have used this characteristic for temperature-insensitive sensing applications [8].

During the writing of R-LPFGs, if larger CO_2-laser energy is applied, an R-LPFG with rotary grooves can be obtained, as shown in Fig. 16. In this case, the rejection bands of the LPFG also split into two. Furthermore, we found that the corresponding wavelength separation was much sensitive to the applied strain. For example, the strain sensitivity of the wavelength separation is almost two orders of magnitude larger than that of conventional LPFGs [7].

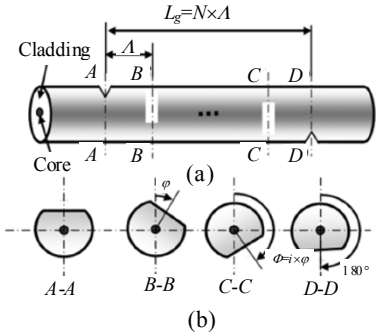

Fig. 16 Structure of a grating with rotary grooves: (a) refractive- index distribution along the fiber axis and (b) refractive-index distribution across the fiber cross section [7].

2.1.4 LPFGs in phonic crystal fibers

The LPFG induced in a solid core PCF by the CO_2 laser has a number of novel features compared to an LPFG in a conventional SMF, such as the low thermal coefficient, high thermal stability, high sensitivity to the refractive index change and stress change.

Recently, we reported the fabrication of an LPFG on a solid-core PCF [9]. Figure 17 gives the transmission spectrum of such an LPFG. We can see the resonant wavelength tends to shift to the longer wavelength with an increased number of scans. Figure 18 shows the temperature response of the LPFG. In the first measurement, the temperature response of the LPFG resonant wavelength is unrepeatable. After being heated to 600 ℃, the heating process and the cooling process almost have the same temperature sensitivity (i.e., 0.0108 nm/℃).

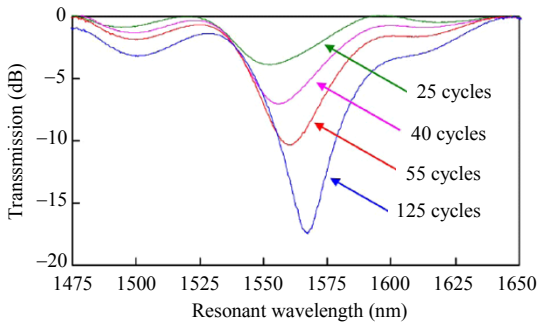

Fig. 17 Transmission spectrum changes in the LPFG written in a PCF with an increase in the scan number [9].

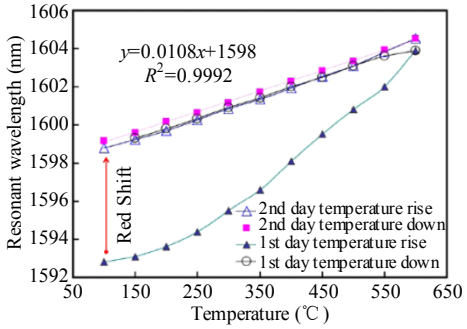

Fig. 18 LPFG resonant wavelength shifts versus temperature [9].

2.1.5 Ultra-long-period fiber grating

The above studies mainly focused on the LPFGs with a typical period of sub-millimeters. In this sub-section, we will introduce the ultra-long-period fiber grating (ULPFG) with periods of up to several millimeters.

One typical transmission spectrum of the ULPFG written by us is given in Fig. 19. It is observed that large resonant peak amplitudes of up to 16 dB ($^4LP_{05}$) are obtained [10]. The responses of the resonant-peak wavelength versus temperature, strain, rotation and refractive index are presented in Figs. 20–23.

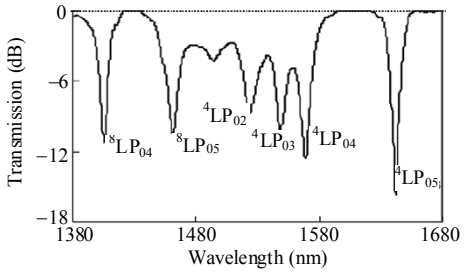

Fig. 19 Transmission spectrum of the ULPFG with a 2-mm period [10].

Figure 20 indicates that different resonant peaks of the ULPFG have different temperature sensitivities, and the relationship between the wavelength shift and temperature is linear. Besides, the changes in the amplitudes of the resonant peaks are very little. Figure 21 indicates that the wavelength sensitivities of $^4LP_{05}$ and $^8LP_{04}$ modes are –0.5 nm/με and –0.25 nm/με, respectively. These temperature and strain characteristics of the ULPFG indicate that simultaneous measurements of both temperature and strain can be realized.

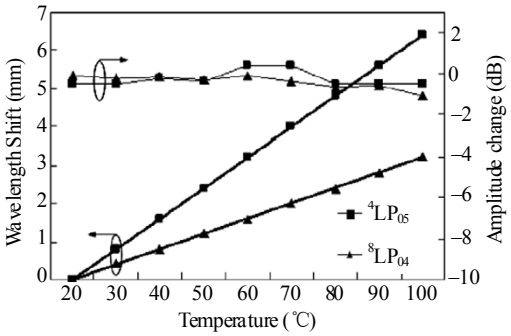

Fig. 20 Temperature response of the ULPFG with a 3-mm period [11].

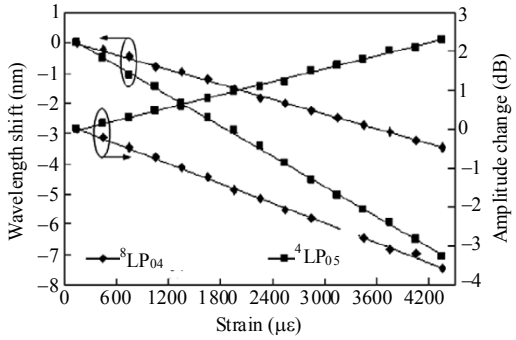

Fig. 21 Strain response of the ULPFG with a 3-mm period [12].

The torsion characteristics of resonant peaks are shown in Fig. 22, which display the linear relationship between the wavelength shift of $^4LP_{05}$ resonant peak and the twist rate. The obtained torsion sensitivity is 0.25 nm/(rad/m), which is 4 times higher than that of the LPFG with a 0.5-mm period fabricated using the high-frequency CO_2 laser pulses technique. It is also found that the resonant wavelength shifts linearly towards the longer wavelength when the ULPFG is twisted clockwise, and the opposite process occurs when the ULPFG is twisted counter-clockwise.

In Fig. 23, we find that the wavelength shift of $^4LP_{05}$ has a nonlinear relationship with the refractive index, and the maximum wavelength shift towards the short wavelength direction is –9 nm for an index change from 1.32 to 1.46. Compared with $^4LP_{05}$, $^8LP_{04}$ is insensitive to the refractive index change.

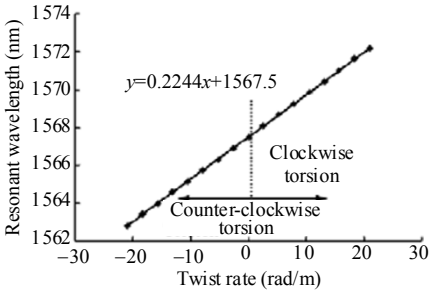

Fig. 22 Relationship between the wavelength shift of the $^4LP_{05}$ resonant peak and the twist rate [13].

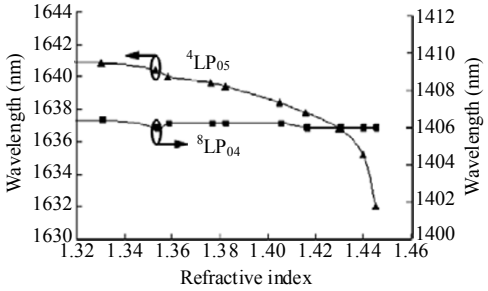

Fig. 23 Relationship between the resonant wavelength shift and refractive index change [12].

2.2 Applications of LPFGs

For the LPFGs fabricated by us using CO_2 lasers, the side-writing method is adopted. We have demonstrated that the LPFGs are sensitive to the temperature, torsion, strain, and outer refractive index in Section 2.1. Moreover, the LPFGs also exhibit some other useful characteristics, i.e., orientation-dependences for the bending and transverse load. Based on these characteristics, various applications of the LPFGs [14–28] are proposed in the following sub-section.

2.2.1 LPFGs for sensing

A. Orientation-dependent sensing of bending

Figure 24 shows the variation of the wavelength shift as a function of the axial rotation angle for a CO_2 laser carved LPFG with a constant bending curvature [14]. It is seen that the bend sensitivity of the wavelength shift varies periodically as a function of the axial orientation angle. There are two positions where the bend sensitivity is minimum, i.e. 72° and 252°, and there are two positions where the bend sensitivity is maximum, i.e. 162° and 342°.

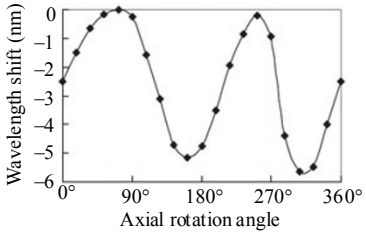

Fig. 24 Wavelength shift as a function of axial orientation for the bending depth of 2.5 mm [14–21].

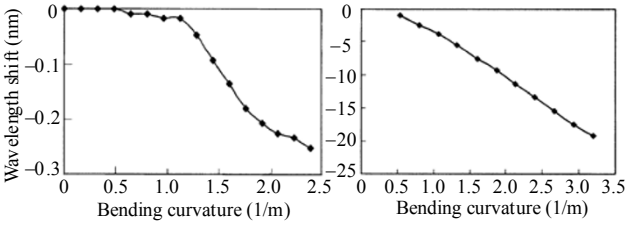

(a) (b)

Fig. 25 Wavelength shift against the bending curvature at two extreme positions with different bend sensitivities: (a) the lowest sensitivity and (b) the highest sensitivity [14].

The central wavelength shifts against the bending curvatures at these special bending directions are shown in Figs. 25(a) and 25(b). In Fig. 25(b), the wavelength shift increases linearly with the bending curvature when the bending direction is at the most bend-sensitive orientation, corresponding to a bend sensitivity of –7 nm/m. However, Fig. 25(a) shows that the central wavelength hardly shifts when the curvature plane is at the most insensitive orientation. This character can be used to develop a bend-insensitive sensor to solve the problem of the cross-sensitivity between bend and other measurands.

B. Sensing of the transverse load

We also investigated the transverse-load characteristics of a twisted LPFG. The experimental setup is shown in Fig. 26. The twisted LPFG is arranged to have different twist ratios by means of first fixing the left rotation disc and then rotating the right rotation disc. The transversal-load characteristics of the twisted LPFG at different orientations are measured by increasing a load F after the left and right rotation discs are rotated with the same angle each time.

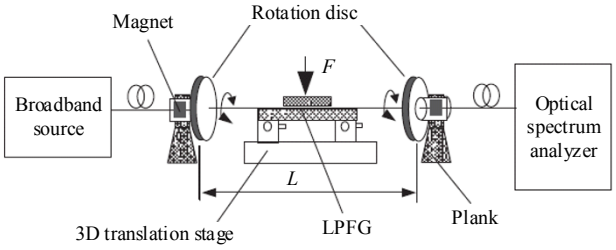

Fig. 26 Experimental setup to test transversal-load characteristics of twisted LPFGs [18].

Figure 27 gives the resonant wavelength shift as a function of the axial rotation angle. Obviously, the orientation-dependence of the twisted LPFG is much smaller than that of the torsion-free LPFG.

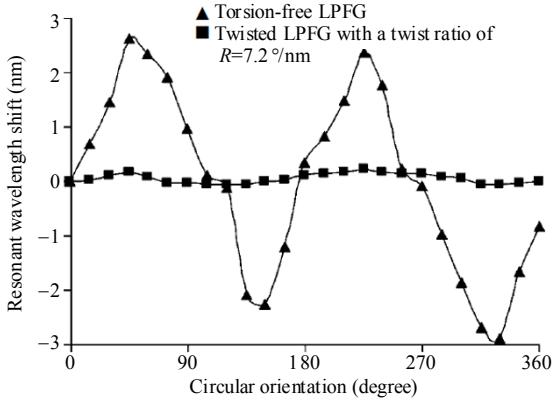

Fig. 27 Relationship between the resonant wavelength shift and circular orientation [18].

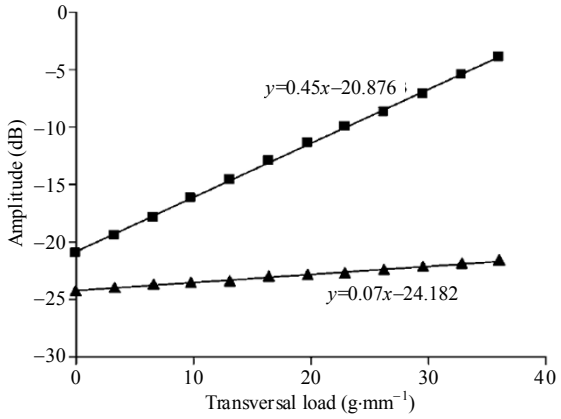

Fig. 28 Relationship between amplitude and applied transverse-load for torsion-free and twisted LPFG [18].

The relationship between the peak amplitude of the LPFG and the applied transversal-load is shown in Fig. 28. It can be seen that the amplitude of the resonant peak of the twisted LPFG has a linear relationship with the transversal load, and its transversal-load sensitivity is about seven times higher than that of the torsion-free LPFG.

C. Multi-parameter measurement

Using the orientation-dependence characteristics of side-writing LPFGs, methods for multi-parameter measurement were developed by us, i.e., simultaneously determining the twist rate and twist direction, simultaneously determining the curvature and bend-direction, and simultaneously measuring the refractive index and temperature [20, 21]. One example is presented in Fig. 29.

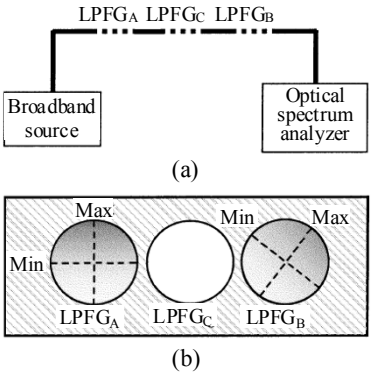

Fig. 29 Schematic diagram of LPFG sensors that can measure the curvature and determine the bend direction simultaneously: (a) the sensor scheme and (b) the cross section of the three LPFGs [20].

The sensor includes three LPFGs. A UV-lasing-written LPFG is set between two CO_2-laser-written LPFGs. As we know, the resonant wavelength of LPFGs induced by the UV/CO_2 laser shifts linearly with the bending, and its bend-sensitivity is independent/dependent on the bend-directions. Therefore, the sensor can not only measure the curvature, but also determine the bend direction. That is, $LPFG_A$ and $LPFG_B$ determine the bend direction and $LPFG_C$ measures the curvature.

2.2.2 LPFGs for other applications

Based on the band rejection characteristics, the variability of the transmission spectrum and especially the orientation-dependent characteristics of the above mentioned LPFGs, we designed novel gain equalizers, couplers as well as filters [22–28].

A. Gain equalizer based on LPFGs

One method of gain equalization proposed by us

is described in Figs. 30 and 31. Figure 30(a) shows the measured transmission spectra of the LPFG for different curvature radii. It can be seen that the dips can be adjusted by the applied curvature. In addition, the bending-caused central wavelength shift can be compensated thermally to match the gain profile, seeing Fig. 30(b). Hence, such a good flexibility and linearity for the control of the LPFG performance can provide a wide dynamic range for the flattening of the gain profile, i.e., the gain of the EDFA, seeing Fig. 31.

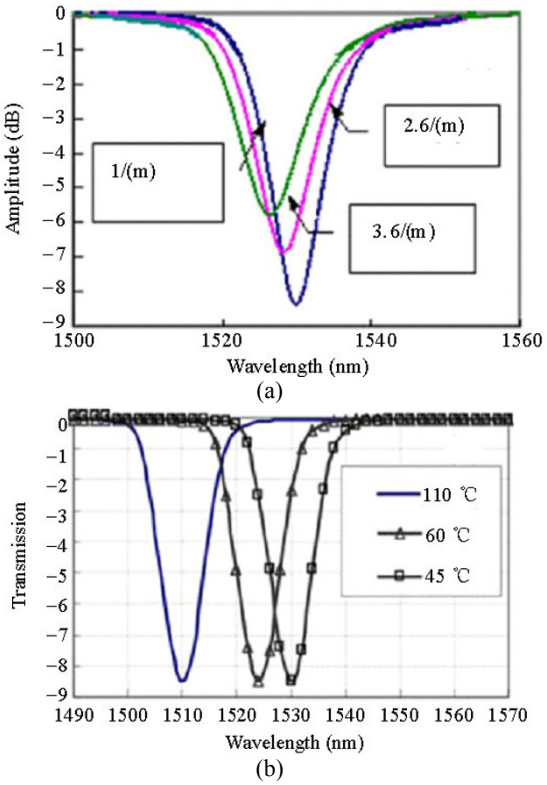

Fig. 30 Measured transmission spectra of the LPFG for different (a) curvature radii and (b) temperatures [23].

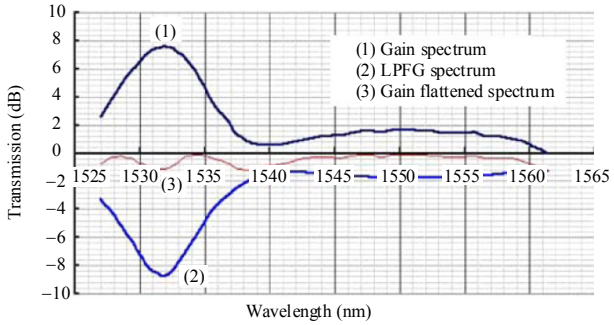

Fig. 31 Experimental results of two EDFAs with gain equalization [23].

Similarly, an LPFG in a bend-insensitive fiber is used to realize dynamics gain equalization. As show in Fig. 32, the peak amplitude of the LPFG can be adjusted dynamically by varying its bending curvature without a significant change in its wavelength [24–26].

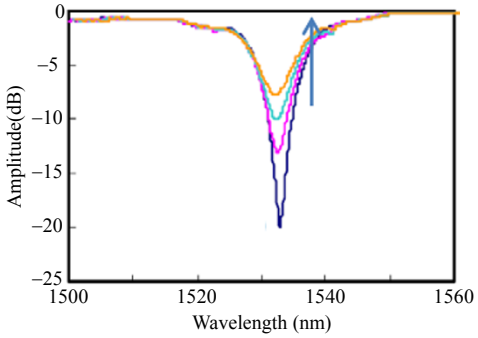

Fig. 32 Transmission spectra of the bend-insensitive fiber based LPFG with different curvatures [24] (as indicated by the arrow, the curves from the bottom up correspond to the curvatures of 0, 0.4 m^{-1}, 0.55 m^{-1} and 0.7 m^{-1}, respectively) [24].

B. Light coupling based on LPFGs

The LPFG formed in an SMF enables light coupling from the guided mode to selected cladding modes at specific wavelengths. When two parallel LPFGs are set close to each other, light launched into one fiber can be coupled into the other fiber through evanescent-field coupling between the cladding modes of the two parallel gratings. Based on this principle, LPFG couplers in conventional SMFs as well as in born-doped fibers were proposed by us [27, 28]. Figure 33 shows the scheme of the LPFG couplers. Due to the side-writing method of the LPFG, there are four kinds of coupling as shown in Fig. 33(b).

For gratings written in conventional SMFs, the coupling efficiency strongly depends on the fiber orientation with the strongest coupling obtained when the exposed sides of the fibers face each other. For gratings written in boron-doped fibers, the coupling efficiency is independent of the fiber orientation. We achieved a peak coupling efficiency of about 86% with gratings written in a boron-doped fiber by setting a suitable surrounding refractive index and offset distance between the two gratings.

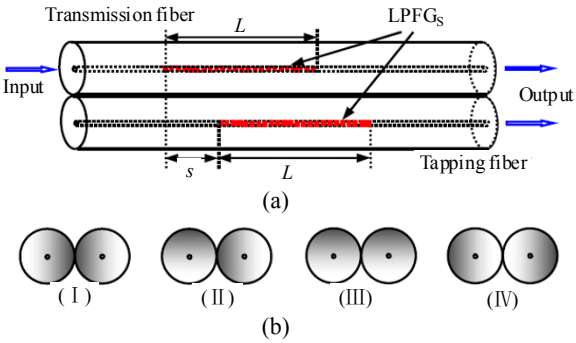

Fig. 33 LPFG couplers: (a) the schematic diagram of two parallel identical LPFGs and (b) four different fiber orientations for the two LPFGs, where the darkened areas represent the sides exposed to the CO_2-laser pulses.

As indicated in Fig. 34, the peak coupling efficiency increases with the offset distance s. The maximum peak coupling efficiency, measured at s= 60 mm with the surrounding index 1.420, is –0.66 dB, corresponding to a power conversion efficiency of 85.9%. To the best of our knowledge, this is the highest experimental coupling efficiency that has ever been reported for an optical coupler using two parallel LPFGs. This result suggests the possibility of realizing efficient broadband all-fiber couplers with CO_2-laser written LPFGs.

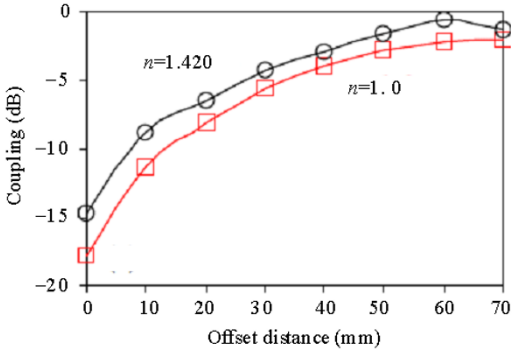

Fig. 34 Dependence of the peak coupling efficiency on the offset distance with the surrounding index n fixed at 1.0 and 1.42 [27].

C. Band-rejection filter based on LPFGs

By combining a normal LPFG and an R-LPFG, we designed a tunable band-rejection filter. The transmission spectra of the normal LPFG and R-LPFG for different torsion rates are given in Figs. 35(a) and 35(b), respectively. For the R-LPFG, the wavelength separation increases with the applied torsion when the direction of the applied torsion is opposite to that of the original twist applied to the fiber (η < 0). On the other hand, the wavelength separation decreases with an increase in the applied torsion when η is greater than 0. For the normal LPFG, the transmission characteristics of the grating are insensitive to the applied torsion and therefore, can be used to compensate for the contrast drop of the R-LPFG.

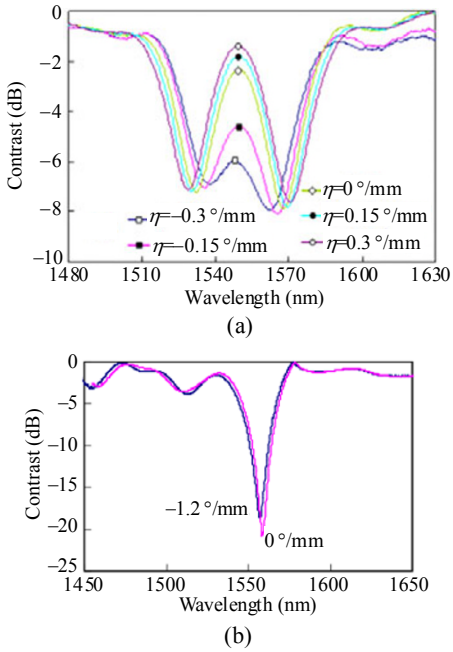

Fig. 35 Transmission spectra of the R-LPFG and the normal LPFG [28].

The combined spectra of the normal LPFG and R-LPFG are given in Fig. 36. It is observed that such a filter shows a bandwidth tuning of about 16.3 nm while keeping a relative high rejection level of about 15 dB.

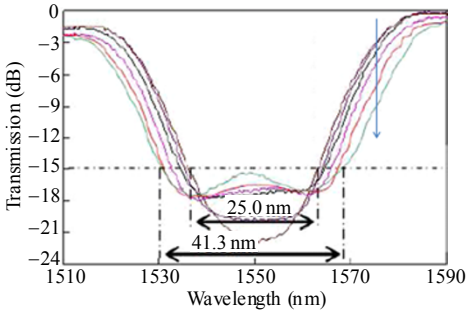

Fig. 36 Transmission spectra of the composite grating at different torsion rates (as indicated by the arrow, the curves from the top down correspond to –1.5 °/mm, –1 °/mm, 0 °/mm, 0.5 °/mm, 1 °/mm and 1.5°/mm, respectively) [28].

3. Studies on the distributed fiber sensor

3.1 Φ-OTDR and P-OTDR

In the Φ-OTDR system, the output of the intrusion detection consists of coherent interference of the signal reflected back from the Rayleigh backscattering within the probe pulse width. If a certain part of the fiber is subjected to a perturbation caused by an intruder, the refractive index of the fiber will be influenced, resulting in a localized optical phase change in the light wave. Hence, the Φ-OTDR can detect perturbations which are too small to be perceived with a conventional OTDR system, making the Φ-OTDR to be a promising technology for intrusion detection [29–33].

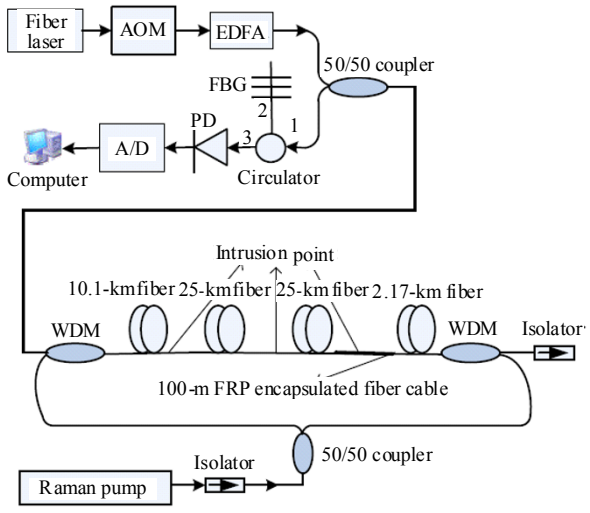

Fig. 37 Experimental setup of the long-distance Φ-OTDR intrusion sensing system [29].

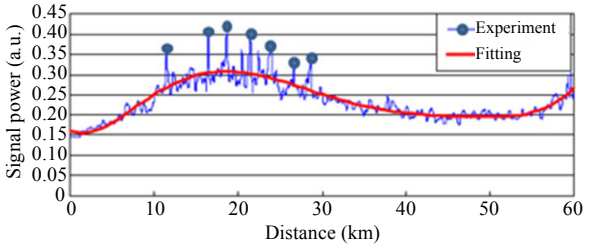

Fig. 38 OTDR signals of bi-directional Raman amplification [29].

To extend the sensing distance, we adopted bi-directional Raman amplification combined with an EDFA in the Φ-OTDR system, and the experimental setup is given in Fig. 37. Figure 38 shows that the signal amplitude distribution along the fiber link is relatively even under bi-directional Raman amplification.

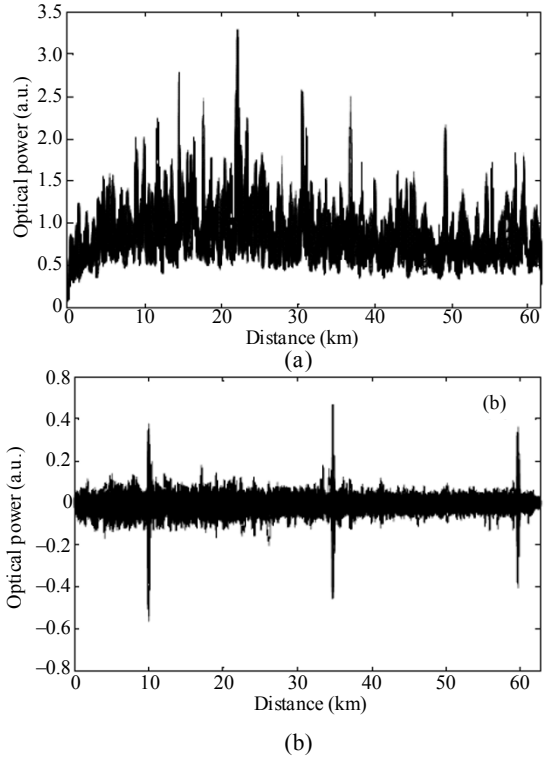

Fig. 39 Experimental results: (a) superposition of 50 consecutive traces and (b) intrusion signals at 10 km, 35 km and 60 km locations [29].

Figures 39(a) and 39(b) respectively give the superposition of 50 consecutive traces and the intrusion signals of the Φ-OTDR system at 10 km, 35 km and 60 km locations after carrying out signal processing to maximize the difference between the background noise level and the intrusion signals. It is seen that such a long distance Φ-OTDR intrusion sensing system can detect intrusions along the whole sensing fiber link of about 62 km with a signal-to-noise ratio of about 7 dB. This is the longest and the most sensitive Φ-OTDR intrusion sensing system reported so far.

To further increase the detection accuracy, a distributed optical fiber intrusion detection system based on the combination of the Φ-OTDR and the POTDR was proposed by us. The corresponding

experimental setup is given in Fig. 40. The backscattered light passing through the port A of a 50/50 coupler is used to examine the spatial distribution of the polarization property by placing a polarization beam splitter (PBS) in front of a photo-detector. The polarization information is converted into the light intensity. In addition, the backscattered light passing through the port B of the 50/50 coupler is used for Φ-OTDR.

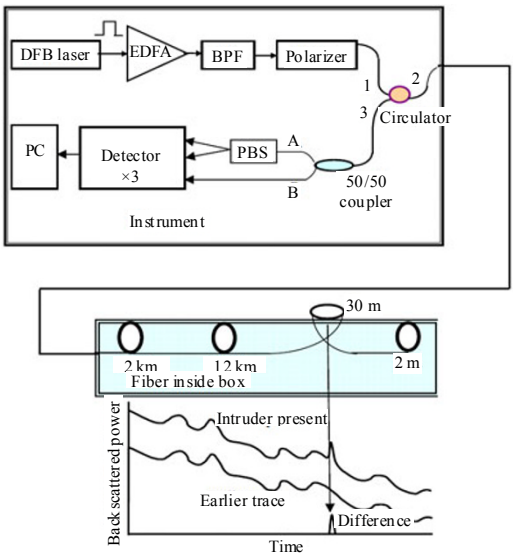

Fig. 40 Configuration of the distributed intrusion detection system base on the combination of the Φ-OTDR and POTDR [32].

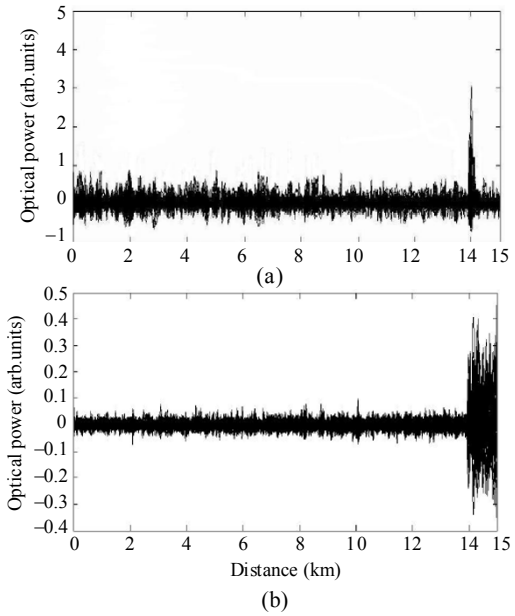

Fig. 41 De-noised signal of the Φ-OTDR [(a)] and POTDR [(b)] by using wavelet transform analysis [32].

In this system, the Φ-OTDR is used to determine the positions of the intrusion by finding peaks, while the POTDR is used to verify the presence of the intrusion and further enhance the probability for judging intrusions, by measuring the density of the signal whose optical power exceeds a threshold pre-set rather than the peaks solely in the Φ-OTDR, as shown in Figs. 41(a) and 41(b). Therefore, it would be ideal to combine the advantages of the two methods in order to achieve multi-point intrusion detection with higher veracity.

3.2 BOTDA

Based on the bi-direction Raman amplification, we also developed a BOTDA system for ultra-long-distance distributed sensing [34, 35]. The system is show schematically in Fig. 42.

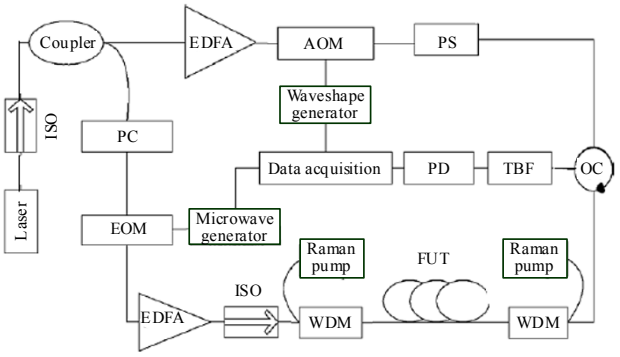

Fig. 42 Experimental setup for long-distance temperature sensing using the BOTDA with Raman amplification [34].

A 1550-nm laser source is split into pump and probe waves after a 90:10 coupler. The first portion is then modulated by an acoustic-optic modulator (AOM), which is driven by the rectangular electrical pulse strain with 1-kHz repetition frequency and 1-s duration time corresponding to 100-m spatial resolution. The continue wave (CW) probe wave is intensity-modulated by an electro-optical modulator (EOM) with 10-GHz bandwidth driven by a microwave generator to create two modulation sidebands at Stokes and anti-Stokes, respectively, while suppressing the carrier by properly setting the DC voltage of the EOM. Both of the pump and

probe waves are pre-amplified by EDFAs before injected into the sensing fiber to compensate for the insertion losses. The Brillouin gain spectrum is acquired after a tunable band-pass filter (TBF) and a photo-detector (PD). In addition, the bi-directional Raman pump configuration pump source is used to amplify signals.

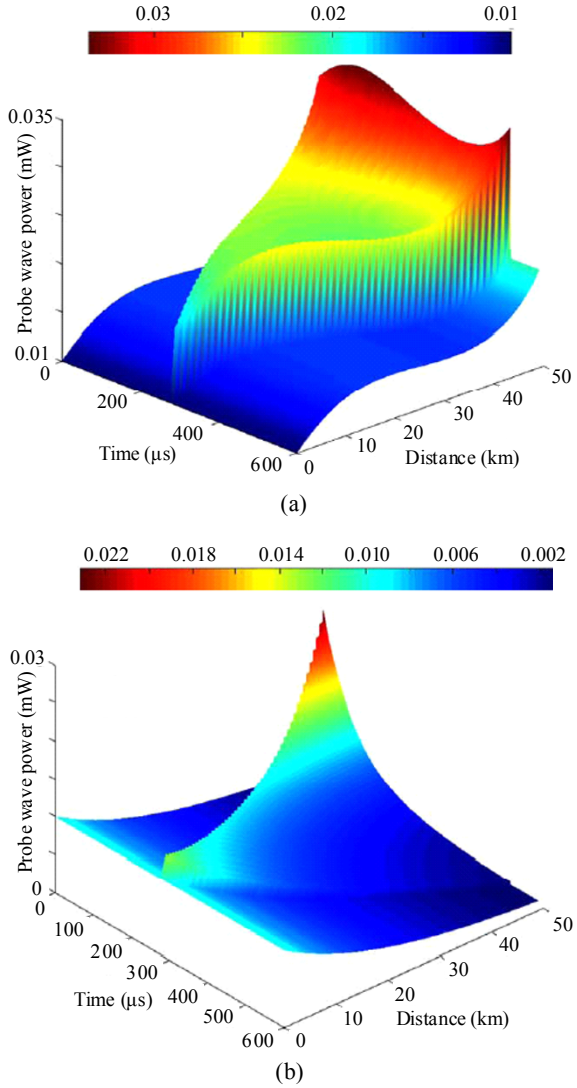

Fig. 43 Intensity evolution over the sensing fiber for the probe wave with [(a)] and without [(b)] bi-directional Raman amplification [34].

Figures 43(a) and 43(b) show respectively the intensity evolution over the sensing fiber for the probe wave with and without bi-directional Raman amplification. Obviously, in the absence of the Raman pump, the power of the probe wave decreases along the sensing fiber exponentially due to fiber loss and pump depletion. Hence, the detected signal-noise ratio (SNR) and measurement accuracy can be enhanced over the whole sensing fiber by using Raman amplification.

A 3D plot of the detected probe wave power versus the sensing distance and frequency difference between the probe and Brillouin pump waves is shown in Fig. 44. A significant Brillouin frequency shift occurs at the heated section. A higher SNR is obtained over the whole sensing fiber owing to the utilization of Raman amplification.

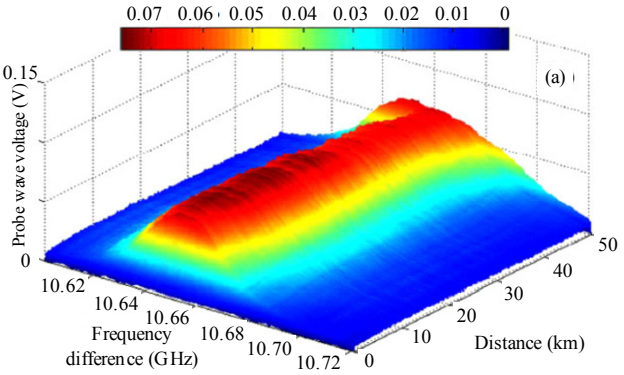

Fig. 44 3D plot of the detected probe wave power versus the sensing distance and frequency difference between probe and Brillouin pump waves [34].

For temperature sensing, we have achieved the sensing length of 75 km. Figure 45(a) illustrates the Brillouin frequency shift as a function of the sensing distance for various temperatures of the heated section. To make it more clear, Fig. 45(b) gives its magnified diagram near the heated section. From these diagrams, the Brillouin frequency shift is increased with the raised temperature accordingly. The measurement accuracy is estimated to be ±0.6 ℃ over the whole sensing fiber. Figure 45(c) displays the Brillouin frequency as a function of temperature at the mid-point of the heated section. The good linear relation is achieved from 35 ℃ to 65 ℃, and the temperature response coefficient is about 1.1 MHz/℃.

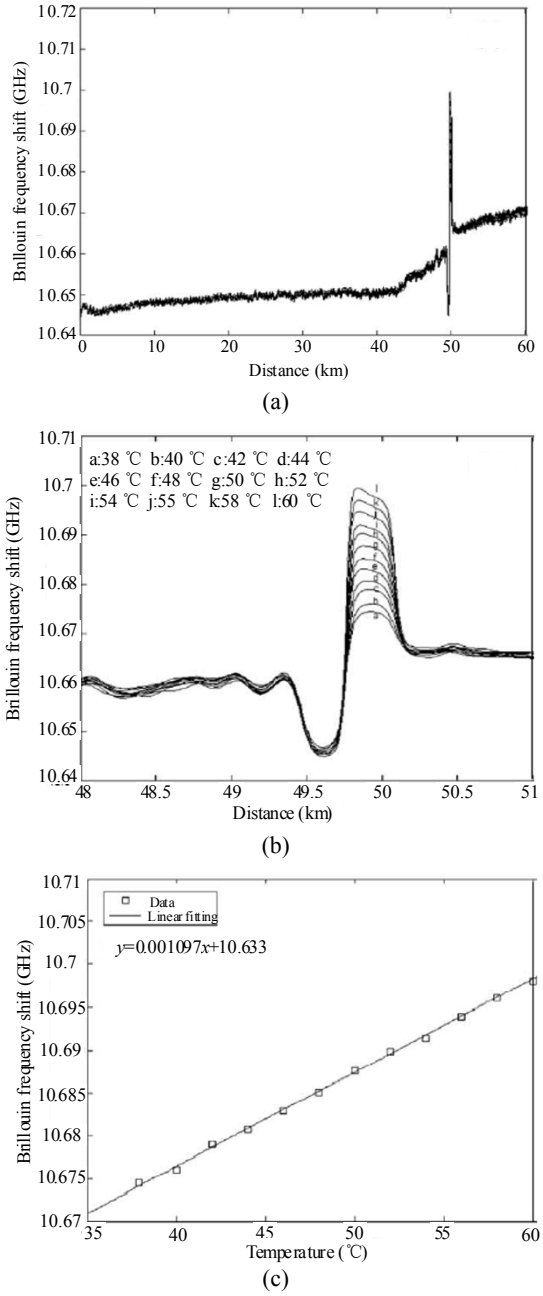

Fig. 45 Distributed temperature sensing through the BOTDA: (a) the Brillouin frequency shift as a function of the sensing distance for various temperatures of the heated section, (b) the magnified diagram of (a) near the heated section, and (c) the Brillouin frequency shift as a function of temperature at the mid-point of the heated section.

Recently, we proposed the use of the optical pulse coding to reduce the frequency uncertainty in a long-distance BOTDA system [35]. The sensing fiber is composed of a 49.6-km fiber at 10.8-GHz Brillouin frequency shift and a 25-km fiber at 11.005-GHz Brillouin frequency shift, as shown in Fig. 46.

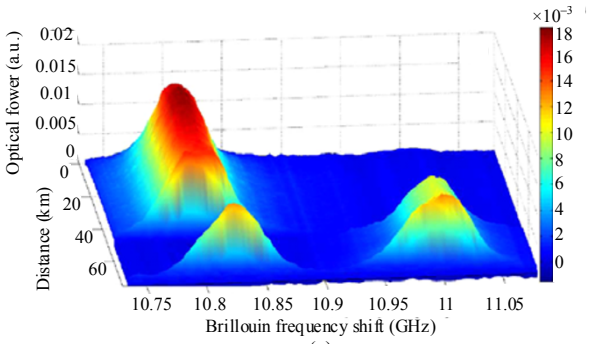

Fig. 46 Decoded optical power distribution for different Brillouin frequency shifts [35].

Comparing Fig. 47(a) with Fig. 47(b), it is

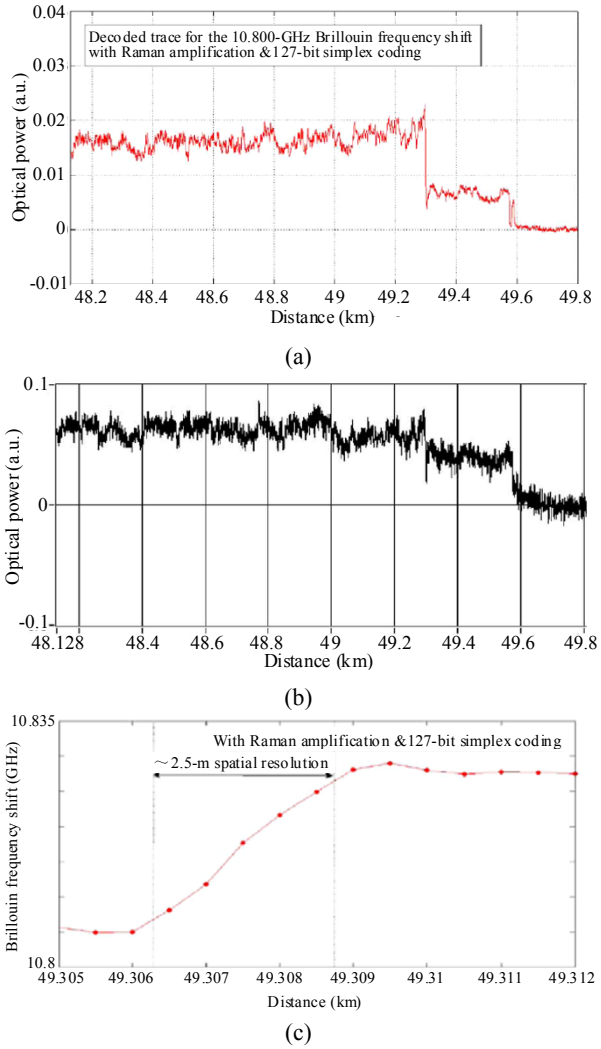

Fig. 47 Experimental result for (a) decoded traces with Raman amplification and optical pulse coding, (b) decoded trace with only Raman amplification, and (c) Brillouin frequency shift distribution near the heated section [35].

obvious that the signal-to-noise ratio is considerably enhanced after introducing the optical pulse coding. Moreover, a relative high special resolution of about 2.5 m is obtained, seeing Fig. 47(c).

4. Studies on microfiber sensors

The microfiber-based sensor is also an important research direction of our recent work. We demonstrated that optical resonators based on microfibers had the large coupling coefficient, low loss and could be used for high-sensitivity sensing [36–38].

4.1 Microfiber temperature sensor

Figure 48 introduces one method we used to form a microfiber knot resonator (MKR). The silica microfibers used were fabricated by flame-heated taper-drawing of a single-mode fiber, while polymer (poly-methyl methacrylate, PMMA) microfibers were fabricated by direct drawing of solvated polymers. These microfibers have minimum diameter of less than 200 nm and length of up to millimeters. They can be bent with much smaller radius of the curvature than that of standard optical fibers to form more compact optical structures. Figures 48(a) and 48(b) show the microscope images of a 190-μm-diameter silica microfiber knot resonator (SMKR) with a 1.7-μm-diameter silica microfiber and a 98-μm-diameter PMMA microfiber knot resonator (PMKR) with a 2.1-μm-diameter PMMA microfiber, respectively.

The MgF_2 crystal plate was adopted as the substrate of the MKR due to its low refractive index and good thermal conductivity. The MKRs were assembled by manipulating with two fiber-tapers under a microscope. The microfiber tapers served as the launching and collecting fibers by evanescent wave coupling. The SMKR/PMKR structures were covered with a thin MgF_2 slab, which provided a gentle means of holding the sensing structure in place and immunity to environment fluctuations.

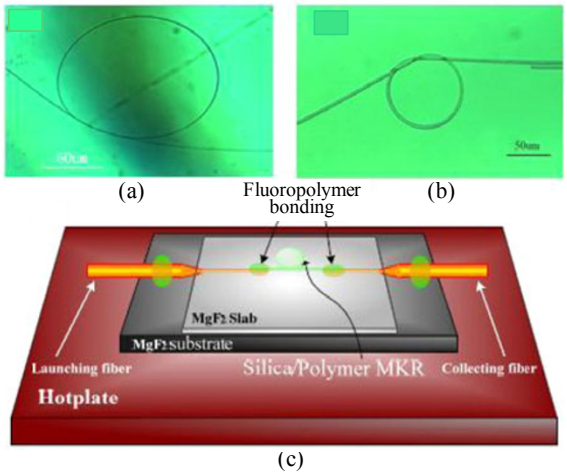

Fig. 48 Microfiber knot resonators and their seeing applications: (a) the photograph of the SMKR, (b) the photograph of the PMKR, and (c) the schematic diagram of the MKRs' temperature sensing structures [36].

The temperature response of the SMKR is shown in Fig. 49. From 420 ℃ to 425 ℃, the total shift of the resonance wavelength is about 260 pm, and the maximum extinction ratio is greater than 10 dB. The relationship between the temperature and resonance wavelength drift over the temperature range from 30 ℃ to 700 ℃ shows good linearity with a sensitivity of 52 pm/℃.

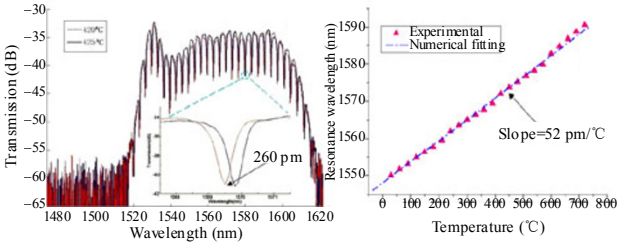

(a) (b)

Fig. 49 Spectra changes in the SMKR for different temperatures: (a) spectra of SMKR at temperature of 420 ℃ and 425 ℃ (the inset shows a single resonance peak) and (b) static temperature response of the SMKR [36].

For the PMKR the measured temperature sensitivity is about 266 pm/℃, which is more than five times larger than that of the SMKR. This is because the thermal expansion coefficient and thermal-optical coefficient of the polymer microfibers are larger than that of the silica microfibers.

4.2 Microfiber acceleration sensor

In our research, the MKR was also used for acceleration sensing by interrogating the vibration of an MEMS structure [37]. As schematically shown in Figs. 50 and 51, the MKR is located at the top surface of the MEMS cantilevers. Both ends of the flexible MKR are connected to SMFs through two fiber tapers. Light is launched into the MKR from the standard fiber through one taper, and the collection fiber is used to receive the light output from the knot via evanescent field coupling. When acceleration is applied to the MOEMS structure, the MKR is influenced by the strain which causes the resonant wavelength of the MKR to shift.

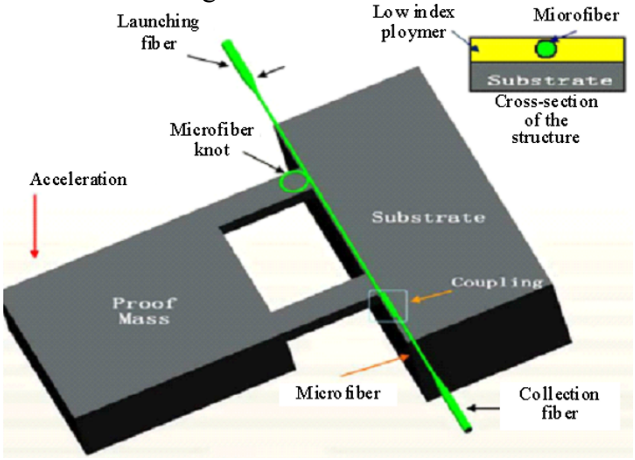

Fig. 50 Schematic of the MKR accelerometer [37].

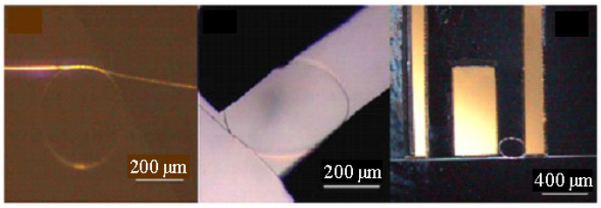

(a) (b) (c)

Fig. 51 MKR and the MKR accelerometer: (a) the photograph of the MKR, (b) thr surface profiler picture of the MKR accelerometer, and (c) the microscope photograph of the MKR accelerometer [37].

The output spectrum of the MKR is shown in Fig. 52(a). The inset of Fig. 52(a) shows that one of the resonant wavelengths shifts by 145 pm with 5*g* applied acceleration. The resonant wavelength shift of the MKR against the applied acceleration is shown in Fig. 52(b). It is seen that the resonant wavelength of the MKR has a good linear relationship with acceleration change in the range of 20*g* with a slope of 29 pm/g. This sensitivity is one order of magnitude larger than that of commercial capacitance-based MEMS accelerometers and most MOEMS accelerometers which have been reported to date.

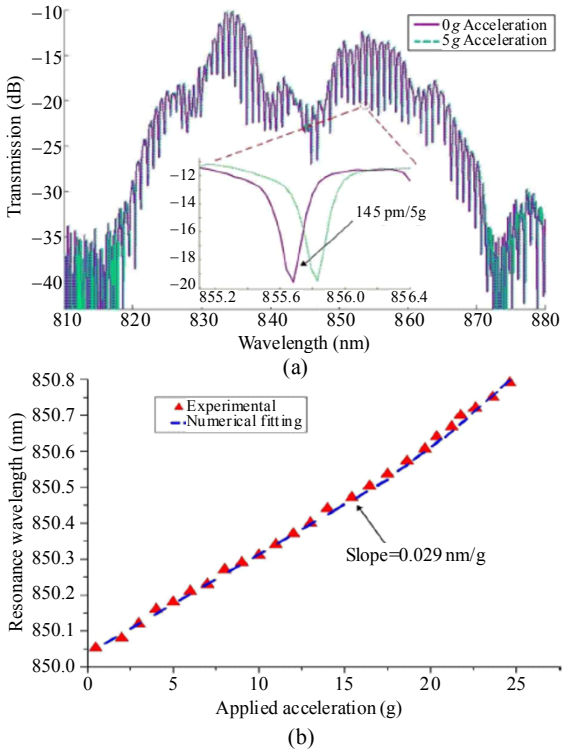

Fig. 52 Spectrum change in the MKR at different values of acceleration: (a) the output spectrum of the MKR accelerometer and (b) the resonance wavelength shift of the MKR accelerometer against the applied acceleration [37].

4.3 Microfiber based interferometer

As a successive work, we proposed and demonstrated an all-fiber high *Q* Mach-Zehnder interferometer coupled microknot resonator structure [38], seeing Fig. 53. The obtained *Q* factor was about 15000, and the interference fringes had an extinction ratio of up to 15 dB.

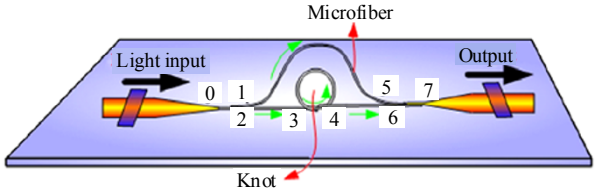

Fig. 53 Schematic diagram of the Mach-Zehnder interferometer coupled microknot resonator structure [38].

5. Summary

Our studies on LPFGs, distributed sensing systems, and microfiber sensors have been reviewed above.

In the fabrication of LPFGs, a novel 2D high-frequency CO_2 laser processing method is adopted. Usually, this method induces an asymmetric refractive index modulation in the fiber. If the dose of the CO_2 laser is relative large, LPFGs with periodical grooves can be formed. In this type of LPFGs, the stretch-induced microbend can effectively enhance the refractive index modulation; hence, the sensitivity of tensile strain for LPFGs with periodical grooves is significantly enhanced.

For LPFGs written in specially doped fibers, the refractive index and the fictive temperature of the glass can be changed differently by different heating or cooling processes, resulting in complex fluctuations of the resonance of LPFGs in the writing process. For LPFGs written in twisted fibers, the R-LPFG with resonance splitting can be obtained. The separation of two split dips is sensitive to torsion but insensitive to temperature, which can be used for the temperature-independent measurement. For LPFGs written in PCFs, their stability, linearity, and repeatability to temperature and tensile strain responses under high temperature conditions can be greatly enhanced by proper annealing. For ULPFGs, their resonant peaks have different temperature/strain sensitivities and can be used to measure temperature and strain simultaneously.

For the applications of LPFGs, the asymmetric index modulation characteristics of LPFGs can be used for bend-insensitive measurement, and twisted LPFGs show much higher sensitivity to the transverse load than normal LPFGs. These characteristics can also be used for multi-parameter measurement, e.g., a cascade structure of LPFGs including two CO_2-laser-carved LPFGs, and a UV-laser-carved LPFG was proposed for simultaneous determination of bend and bend direction. In addition, the band-rejection characteristics of LPFGs and their tunability were also used to form the gain equalizer, optical coupler, and band-pass filter.

For distributed sensing systems, our research covered Φ-OTDR, POTDR and BOTDA. To increase the sensing distance, we proposed the use of bi-directional Raman amplification combined with EDFAs. To increase the detection accuracy, the combination of the Φ-OTDR and POTDR was proposed. It was verified that our Φ-OTDR intrusion sensing system could detect intrusions along the whole sensing fiber link of about 62 km with a signal-to-noise ratio of about 7 dB, which was the longest and the most sensitive Φ-OTDR intrusion sensing system reported so far. For the BOTDA system, we have achieved the sensing length of 75 km with a temperature resolution of ±0.6 ℃. In addition, optical pulse coding has been used in the BOTDA system to enhance the signal-to-noise ratio greatly.

For microfiber sensors, we mainly focused on the MKRs. The MKRs made from silica and polymer exhibiting relatively high temperature sensitivity of 52 pm/℃ and 266 pm/℃, respectively. The MKRs had a acceleration sensitivity of 29 pm/g, which was one order of magnitude larger than that of commercial capacitance-based MEMS accelerometers.

Acknowledgement

The author would like to acknowledge the group members at University of Electronic Science and Technology of China and Chongqing University, and the support of Education Ministry and National Science Foundation of China.

References

[1] Y. J. Rao, "Studies on fiber optic low-coherence interferometric and fiber Brag grating sensors," *Photonic Sensors*, vol. 1, no. 4, 382–400, 2011.

[2] Y. J. Rao, Y. P. Wang, Z. L. Ran, and T. Zhu, "Novel fiber-optic sensors based on long-period fiber gratings written by high-frequency CO_2 laser pulses," *Journal of Lightwave Technology*, vol. 21, no. 5, pp. 1320–1327, 2003.

[3] T. Zhu, Y. J. Rao, J. L. Wang, and Y. Song, "A highly sensitive fiber-optic refractive index sensor based on an edge-written long-period fiber grating," *IEEE Photonics Technology Letters*, vol. 19, no. 24, pp. 1946–1948, 2007.

[4] Y. P. Wang, D. N. Wang, W. Jin, Y. J. Rao, and G. D. Peng, "Asymmetric long period fiber gratings fabricated by use of CO_2 laser to carve periodic grooves on the optical fiber," *Applied Physics Letters*, vol. 89, no. 15, pp. 151105, 2006.

[5] Y. Liu, H. W. Ho, K. S. Chiang, T. Zhu, and Y. J. Rao, "Glass structure changes in CO_2-laser writing of long-period fiber gratings in Boron-doped single-mode fibers," *Journal of Lightwave Technology*, vol. 27, no. 7, pp. 857–863, 2009.

[6] Y. Gu, K. S. Chiang, and Y. J. Rao, "Writing of apodized phase-shifted long-period fiber gratings with a computer-controlled CO_2 laser," *IEEE Photonics Technology Letters*, vol. 21, no. 10, pp. 657–659, 2009.

[7] T. Zhu, Y. J. Rao, Y. Song, K. S. Chiang, and M. Liu, "Highly sensitive temperature-independent strain sensor based on a long-period fiber grating with a CO_2-laser engraved rotary structure," *IEEE Photonics Technology Letters*, vol. 21, no. 8, pp. 543–545, 2009.

[8] T. Zhu, K. S. Chiang, Y. J. Rao, C. H. Shi, Y. Song, and M. Liu, "Characterization of long-period fiber gratings written by CO_2 laser in twisted single-mode fibers," *Journal of Lightwave Technology*, vol. 27, no. 21, pp. 4863–4869, 2009.

[9] Y. J. Rao, D. W. Duan, Y. E. Fan, T. Ke, and M. Xu, "High-temperature annealing behaviors of CO_2 laser pulse-induced long-period fiber grating in a photonic crystal fiber," *Journal of Lightwave Technology*, vol. 28, no. 10, pp. 1530–1535, 2010.

[10] Y. J. Rao, T. Zhu, and Q. J. Mo, "Highly sensitive fiber-optic torsion sensor based on an ultra-long-period fiber grating," *Optics Communications*, vol. 266, no. 1, pp. 187–190, 2006.

[11] T. Zhu, Y. J. Rao, and Q. J. Mo, "High sensitivity fiber-optic torsion sensor based on a novel ultra long-period fiber grating," *Acta Physica Sinica*, vol. 55, no. 1, pp. 249–253, 2006 (in Chinese).

[12] T. Zhu, Y. J. Rao, Q. J. Mo, and J. L. Wang, "Study on characteristics of a CO_2-laser-induced ultra-long-period fiber grating," *Acta Physica Sinica*, vol. 56, no. 9, pp. 5287–5292, 2007 (in Chinese).

[13] T. Zhu, Y. J. Rao, and J. L. Wang, "Characteristics of novel ultra-long-period fiber gratings fabricated by high-frequency CO_2 laser pulses," *Optics Communications*, vol. 277, no. 1, pp. 84–88, 2007.

[14] Y. P. Wang, Y. J. Rao, Z. L. Ran, T. Zhu, and X. K. Zeng, "Bend-insensitive long-period fiber grating sensors," *Optics and Lasers in Engineering*, vol. 41, no. 1, pp. 233–239, 2004.

[15] Y. P. Wang and Y. J. Rao, "Long period fiber grating torsion sensor measuring twist rate and determining twist direction simultaneously," *Electronics Letters*, vol. 40, no. 3, pp. 164–166, 2004.

[16] Y. P. Wang and Y. J. Rao, "CO_2-laser induced LPFG torsion characteristics depending on length of twisted fiber," *Electronics Letters*, vol. 40, no. 18, pp. 1101–1103, 2004.

[17] T. Zhu, Y. J. Rao, J. L. Wang, and M. Liu, "Transverse-load characteristics of twisted long-period fiber gratings written by high-frequency CO_2 laser pulses," *Electronics Letters*, vol. 42, no. 8, pp. 21–22, 2006.

[18] Y. P. Wang, J. P. Chen, and Y. J. Rao, "Torsion characteristics of long-period fiber gratings induced by high-frequency CO_2 laser pulses," *Journal of the Optical Society of America B: Optical Physics*, vol. 22, no. 6, pp. 1167–1172, 2005.

[19] Y. P. Wang, D. N. Wang, W. Jin, and Y. J. Rao, "Asymmetric transverse-load characteristics and polarization dependence of long-period fiber gratings written by a focused CO_2 laser," *Applied Optics*, vol. 46, no. 16, pp. 3079–3086, 2007.

[20] Y. P. Wang and Y. J. Rao, "A novel long period fiber grating sensor measuring curvature and determining bend-direction simultaneously," *IEEE Sensors Journal*, vol. 5, no. 5, pp. 839–843, 2005.

[21] T. Zhu, Y. J. Rao, and Q. J. Mo, "Simultaneous measurement of refractive index and temperature using a single ultralong-period fiber grating," *IEEE Photonics Technology Letters*, vol. 17, no. 12, pp. 2700–2702, 2005.

[22] Y. P. Wang, Y. J. Rao, Z. L. Ran, T. Zhu, and A. Z. Hu, "A novel tunable gain equalizer based on a long-period fiber grating written by high-frequency CO_2 laser pulses," *IEEE Photonics Technology Letters*, vol. 15, no. 2, pp. 251–253, 2003.

[23] Y. J. Rao, T. Zhu, Z. L. Ran, Y. P. Wang, J. Jiang, and A. Z. Hu, "Novel long-period fiber gratings written by high-frequency CO_2 laser pulses and applications in optical fiber communication," *Optics Communications*, vol. 229, no. 1–6, pp. 209–221, 2004.

[24] Y. J. Rao, A. Z. Hu, and Y. C. Niu, "A novel dynamic LPFG gain equalizer written in a bend-insensitive fiber," *Optics Communications*, vol. 244, no. 1–6, pp. 137–140, 2005.

[25] T. Zhu, Y. J. Rao, R. K. Wang, and J. L. Wang, "All fiber dynamic gain equalizer based on a fiber grating

with rotary refractive index change," *Acta Physica Sinica*, vol. 55, no. 9, pp. 4720–4724, 2006 (in Chinese).

[26] T. Zhu, Y. J. Rao, and J. L. Wang, "All-fiber dynamic gain equalizer based on a twisted long-period grating written by high-frequency CO_2 laser pulses," *Applied Optics*, vol. 46, no. 3, pp. 375–378, 2007.

[27] Y. Q. Liu, K. S. Chiang, Y. J. Rao, Z. L. Ran, and T. Zhu, "Light coupling between two parallel CO_2-laser written long-period fiber gratings," *Optics Express*, vol. 15, no. 26, pp. 17645–17651, 2007.

[28] T. Zhu, C. H. Shi, Y. J. Rao, L. L. Shi, and K. S. Chiang, "All-fiber bandwidth-tunable band-rejection filter based on a composite grating induced by CO_2 laser pulses," *Optics Express*, vol. 17, no. 19, pp. 16750–16755, 2009.

[29] Y. J. Rao, J. Luo, Z. L. Ran, J. F. Yue, X. D. Luo, and Z. Zhou, "Long-distance fiber-optic Φ-OTDR intrusion sensing system," in *Proc. SPIE (The International Society for Optical Engineering*, *20th International Conference on Optical Fiber Sensors)*, vol. 7503, pp. 75031O, 2009.

[30] K. L. Xie, Y. J. Rao, and Z. L. Ran, "Distributed optical fiber sensing system based of Rayleigh scattering light Φ-OTDR using single-mode fiber laser with high power and narrow linewidth," *Acta Optica Sinica*, vol. 28, no. 3, pp. 569–572, 2008 (in Chinese).

[31] J. Luo, Y. J. Rao, J. F. Yue, and Z. L. Ran, "Highly sensitive distributed optical fiber intrusion monitoring system," *Chinese Journal of Scientific Instrument*, vol. 30, no. 6, pp. 1123–1128, 2009 (in Chinese).

[32] Y. J. Rao, J. Z. Li, Z. L. Ran, and K. L. Xie, "Distributed intrusion detection based on combination of Φ-OTDR and POTDR," in *Proc. SPIE (The International Society for Optical Engineering*, *19th International Conference on Optical Fiber Sensors)*, vol. 7004, pp. 700461, 2008.

[33] Z. L. Ran, Y. J. Rao, L. W. Luo, S. Xiong, and Q. Deng, "Φ-OTDR used for providing security service in EPON," in *OECC* (*14th OptoElectronics and Communications Conference)*, pp. 5213305, 2009.

[34] X. H. Jia, Y. J. Rao, L. Chang, C. Zhang, and Z. L. Ran, "Enhanced sensing performance in long distance brillouin optical time-domain analyzer based on Raman amplification: Theoretical and experimental investigation," *Journal of Lightwave Technology*, vol. 28, no. 11, pp. 1624–1630, 2010.

[35] Y. J. Rao, X. H. Jia, L. Li, and Z. L. Ran, "Detailed investigation on gain-clamping characteristics of ultralong fiber Raman laser using FBGs," *Journal of the Optical Society of America B: Optical Physics*, vol. 26, no. 7, pp. 1334–1340, 2009.

[36] Y. Wu, Y. J. Rao, Y. H. Chen, and Y. Gong, "Miniature fiber-optic temperature sensors based on silica/polymer microfiber knot resonators," *Optics Express*, vol. 17, no. 20, pp. 18142–18147, 2009.

[37] Y. Wu, X. Zeng, Y. J. Rao, Y. Gong, C. Hou, and G. Yang, "MOEMS accelerometer based on microfiber knot resonator," *IEEE Photonics Technology Letters*, vol. 21, no. 20, pp. 1547–1549, 2009.

[38] Y. H. Chen, Y. Wu, Y. J. Rao, and Y. Gong, "Hybrid Mach-Zehnder interferometer and knot resonator based on silica microfibers," *Optics Communications*, vol. 283, no. 14, pp. 2953–2956, 2010.